



Fracture properties of thin film TiN at elevated temperatures

J. Buchinger^{a,*}, L. Löfler^b, J. Ast^c, A. Wagner^a, Z. Chen^d, J. Michler^c, Z.L. Zhang^d, P.H. Mayrhofer^a, D. Holec^b, M. Bartosik^a

^a Institute of Materials Science and Technology, TU Wien, Getreidemarkt 9, Vienna A-1060, Austria

^b Department of Materials Science, Montanuniversität Leoben, Leoben A-8700, Austria

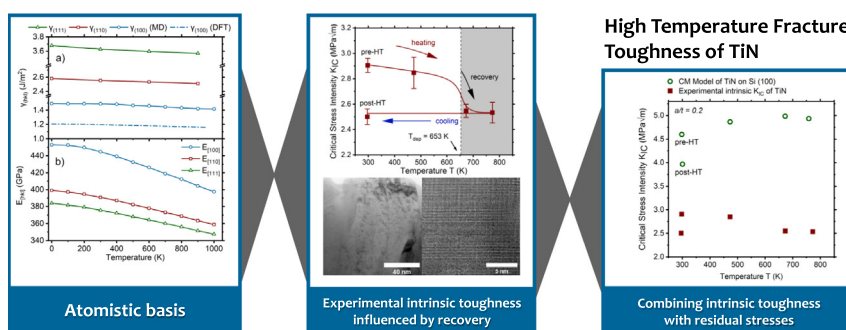
^c Empa, Swiss Federal Laboratories for Materials Science and Technology, Laboratory for Mechanics of Materials and Microstructures, Feuerwerkerstr. 39, 3602 Thun, Switzerland

^d Erich Schmid Institute of Materials Science, Austrian Academy of Sciences, Jahnstraße 12, Leoben, A-8700, Austria

HIGHLIGHTS

- Temperature-dependent molecular dynamics calculations of the (100), (110), and (111) surface energies of TiN.
- In situ microcantilever bending tests performed at ambient, and elevated temperatures.
- Growth defect recovery identified as a decreasing factor for the fracture toughness of TiN thin films.
- Analytical continuum mechanics model consulted to estimate the temperature-dependent apparent fracture toughness of TiN attached to a Si substrate.

GRAPHICAL ABSTRACT



ARTICLE INFO

Article history:

Received 27 March 2020

Received in revised form 15 May 2020

Accepted 12 June 2020

Available online 13 June 2020

Keywords:

High temperature micromechanics

Transition metal nitrides

Thin films

Sputtering

Molecular dynamics

Continuum mechanics

ABSTRACT

We provide an experimental and theoretical description of the high temperature fracture behaviour of TiN thin films. For this, we employ molecular dynamics and density functional theory, to show that the surface energies drop insignificantly between 0 and 1000 K. We utilise these results to predict a slight decrease of the fracture toughness over the aforementioned temperature range.

For the experimental perspective, we use unbalanced DC reactive magnetron sputtering to synthesise a TiN film, on which we perform in situ high temperature microcantilever bending tests. Upon increasing the testing temperature from room temperature to 773 K our results present a slight, irreversible decrease of K_{IC}, once the deposition temperature of the film (~653 K) is exceeded.

Based on our theoretical groundwork, as well as complementary data produced by X-ray diffraction, nanoindentation, transmission electron microscopy, and wafer curvature measurements, we identify growth defect recovery as the main reason behind the decrease of K_{IC}. We observe no change in the deformation and/or fracture mechanism of TiN across the experimentally investigated temperature range. Using an analytical model based on continuum mechanics, we estimate the influence of macro residual stresses on the temperature-dependent fracture toughness of TiN attached to a Si (100) wafer.

© 2020 The Authors. Published by Elsevier Ltd. This is an open access article under the CC BY license (<http://creativecommons.org/licenses/by/4.0/>).

1. Introduction

Mechanical properties at elevated temperatures are a thoroughly explored field in the case of bulk materials [1–4]. Temperature-dependent fracture characteristics have been described and evaluated for a variety

* Corresponding author.

E-mail address: julian.buchinger@tuwien.ac.at (J. Buchinger).

of materials, including bulk-sized alloys, and metallic glasses, as well as micro-sized samples of Si, and W [5–9]. In the case of ceramic thin films, however, the high temperature (HT) fracture behaviour in particular presents itself as rather uncharted territory. Among this family of materials, TiN has garnered widespread popularity within the field of micro-electronics [10–12], fuel cells & batteries [13,14], and as protective coatings against harsh environments [15,16]. In many of these applications, TiN is exposed to severe thermally and/or mechanically-induced stresses [17]. Hence, it is imperative that we expand our understanding of the fracture properties of TiN at elevated temperatures. Furthermore, TiN is commonly consulted as a reference material for the family of refractory nitride and carbide thin films and may therefore serve as a basis to elucidate the fracture mechanisms of other isostructural representatives of this class of materials.

Compared to other, more easily accessible, mechanical properties (e.g. hardness, elastic moduli), studies on the fracture toughness of transition metal nitrides (TMNs) are relatively rare even at ambient temperature. Traditionally, the data available has been produced using classical indentation-based methods [18–20]. However, these procedures can often yield an unsatisfactory degree of accuracy, due to the comparably complex and multiaxial stress state induced by the indenter, potentially unclear crack geometries, and the presence of residual stresses [18,19]. Thus, more sophisticated micromechanical techniques have been developed, including pillar splitting [21], and single cantilever bending tests performed on free-standing film material [22]. Both approaches, which minimise the influence of substrate-related residual stresses, have been applied to determine the fracture toughness of a select few TMNs [23–25], as well as to explore strategies that enhance the intrinsically poor toughness-related properties of TiN and its relatives [26,27]. Microcantilever bending tests have also been conducted to determine the effect of annealing on the critical stress intensity K_{IC} of TiN, TiAlN, and TiN/CrN superlattices [23,28].

In situ micromechanical experiments focusing on the fracture toughness at elevated temperatures have been performed on a small minority of materials. Highlights include the observation of a brittle-to-ductile transition in both Si [8,29] and single-crystalline W [9], due to increasing temperature. Such investigations remain a scarce resource for TMNs however, and the few studies that do exist, possess limited informative value for TMNs as a whole. The scarcity of such studies is predominantly related to the fact that the required experimental equipment has only become available and accessible in recent years. Microcantilever bending tests at elevated temperatures of CrN thin films were assumed to be affected by diffusion of Ga ions (implanted during fabrication of the cantilevers) [30]. For the same material, the micropillar splitting approach was found to gradually lose its validity with increasing temperature, due to deformation of the outer pillar circumference at the higher end of the studied temperature range [31].

Providing a theoretical perspective on the temperature dependence of the mechanical properties of TiN, ab initio molecular dynamics (MD) calculations, performed by Steneteg et al. [32], show that the shear, bulk, and Young's moduli all decrease across a temperature span ranging from 300 K to 1800 K. Similarly, Shulumba et al. [33] reported, based on Density Functional Theory (DFT) calculations, a decrease of all elastic constants of TiAlN upon elevating the temperature from 0 K to 2000 K. Notably, theoretical studies on the temperature dependence of more toughness-relevant quantities are effectively untraceable. In fact, potentials for classical MD calculations of TiN have only become available relatively recently [34,35]; similarly, ab initio MD simulations of reasonably sized models have become feasible also only in the past couple of years. Since then, significant studies have emerged, detailing strength and toughness-related properties of transition metal nitrides from the perspective of ab initio molecular dynamics [36,37].

With both in situ micromechanical experiments at elevated temperatures and temperature-dependent toughness data obtained within the frameworks of DFT and MD simulations at the root of this study, we therefore aim to provide a critical jigsaw piece, propelling us towards

a more comprehensive description of the mechanical characteristics of TiN at application-relevant temperatures. The role of macro residual stresses on the film-substrate system fracture toughness is discussed for TiN on Si (100) using an analytical model estimating the stress intensity for a crack in a thin film on a substrate as a function of crack length and the difference in elastic properties of the film and substrate [38].

2. Methodology

2.1. Computational

The temperature dependent surface energy γ_{hkl} was calculated for the three main crystallographic directions (100), (110) and (111) using molecular dynamics (MD). A modified embedded atom method (MEAM) potential, designed for TiN surface properties, was used [34,35]. The simulations were performed in a large-scale atomic/molecular massively parallel simulator (LAMMPS) [39]. To obtain the surface energy, a block of TiN was relaxed at each given temperature with periodic boundary conditions. For each configuration and temperature, the same initial cell, without the created surface, was run under the same conditions. An NPH (constant number, pressure, and enthalpy) barostat (switched to Parrinello-Rahman) with 1 bar of pressure was applied for the calculations and used for the free energy calculations. The temperature was controlled over a Langevin thermostat set to the desired temperature. After the initial run, the block was separated in the middle, normal to the desired surface and relaxed again. In case of (100) and (110), two identical surfaces, in case of (111), both a nitrogen and a titanium terminated surface are created as it would when a cracks forms in this plane. Each cell consists of 8000–10,000 atoms, the chosen timestep is 0.1 fs with a total simulation time of 5 ps. After roughly 600 fs the target temperature is reached. The surface energy was then calculated from the energy difference according to Eq. 1.

$$\gamma_{hkl}(T) = \frac{E_{slab}(T) - E_{bulk}(T)}{2A}, \quad (1)$$

where E_{slab} and E_{bulk} are the potential energies of the separated and bulk material, respectively, at the given temperature, and A is the area of one of the created surfaces. To validate the results of the MD simulations, γ_{100} was additionally calculated with density functional theory (DFT) using the Generalised Gradient Approximation (GGA) with Projector Augmented Wave (PAW) potentials [40] with a GGA potential in the Vienna ab-initio simulation package (VASP) [41,42]. The phonon frequencies of TiN slabs with different thicknesses were evaluated within the finite displacement method framework implemented in phonopy [43]. Resulting harmonic approximation-based free energy was employed in Eq. 1 to obtain the temperature-dependent surface energy. For the temperature dependent elastic constants, the results of Shulumba et al. were used [33].

From the directional Young's moduli, $E_{[hkl]}$, and corresponding surface energies, $\gamma_{(hkl)}$, the fracture toughness (K_{IC}) is estimated by the following equation, in compliance with [44,45]:

$$K_{IC}(hkl) = \sqrt{4E_{[hkl]}\gamma_{(hkl)}}, \quad (2)$$

2.2. Experimental

All samples discussed in this study were synthesised by unbalanced DC reactive magnetron sputtering inside an adapted lab-scaled Leybold Heraeus Z400. We used Si (100) wafers as substrates, which we ultrasonically cleaned in acetone and ethanol for 5 min each, before mounting them in the stationary substrate holder. The system was subsequently evacuated to a base pressure of roughly 10^{-4} Pa, before thermal purging of the chamber was conducted at 773 K for 20 min. To remove native oxide layers from the surface, the substrates were

ion-etched for 15 min in a pure Ar atmosphere with a pressure of 6 Pa by applying a voltage of -150 V with a frequency of 150 kHz to the substrates. To minimise oxygen contamination of our films, we also adhered to the recommendations of Riedl et al. [46], which have been shown to reduce the level of oxygen contamination below the detection limit of elastic recoil detection analysis (ERDA) in Hf-Ta-Ti-V-Zr nitrides [47] synthesised in the exact same deposition system as the TiN of the present study. These recommendations included sputter-cleaning the Ti target behind the closed shutter for the last 2 min of the etching process in pure Ar. For the deposition process itself, we applied a constant current of 1 A to a 3-in. Ti target, while bleeding a $N_2:Ar$ gas mixture of 12 sccm/28 sccm into the chamber. The total chamber pressure was kept constant at 0.4 Pa. A constant bias voltage of -40 V was applied to the substrates to facilitate the formation of a dense microstructure within our TiN film. We set the substrate heater to 773 K, which resulted in an effective temperature of approximately 653 K on the surface of the substrate (in the following denoted as “deposition temperature”).

To prepare the samples for the cantilever fabrication process, we removed the Si (100) substrate beneath a polished edge of the coating, producing roughly 10 μm of freestanding film material. This was achieved by submerging the sample in a 30% KOH solution heated to 343 K for 2 h. A rotating oblong magnet provided a constant stirring motion. The microcantilevers were cut into the freestanding part of the film using a focussed ion beam (FIB) workstation (FEI Quanta 200 3D DFIB). The rough shape of the cantilevers was prepared with an ion beam current of 3 nA. For the finer patterning steps, producing the final shape of the cantilevers, a current of 500 pA was used, while aiming for dimensions of $t \times t \times 7t$, whereby t denotes the film thickness. We further reduced the current to 50 pA to cut the notches. Our TiN film had a thickness of approximately 2.8 μm , while the cuts for the notches reached a depth of about 470 nm. Thin material bridges were left intact, flanking the notches. All cuts were made using an accelerating voltage of 30 kV. In an effort to minimise drift during the FIB procedure, we sputtered 8 nm of a AuPd alloy (60:40) onto the sample surface.

Microcantilever fracture testing was performed on freestanding film material at ambient and elevated temperatures using a high temperature setup (Alemnis nanoindenter, Alemnis AG, Thun/Switzerland) equipped with a cono-spherical diamond indenter (1 μm tip radius). The experiments were conducted at room temperature, ~ 200 °C (473 K), ~ 400 °C (673 K), ~ 500 °C (773 K), and again at room temperature afterwards. Either 6 or 7 microcantilevers were tested at every temperature. The tip temperature was calibrated by performing indents into a Cu stub at different temperatures covering the investigated temperature range. Prior to the experiments, the contact drift was minimised by adjusting the sample and tip temperature and by performing shallow indentations into the bulk material next to the micro-cantilevers. Further details of this method can be found elsewhere [48]. Drift rates of below 10 nm/min could be achieved. The tests were performed displacement-controlled with a rate of 30 nm/s and were manually interrupted once fracture had occurred.

The dimensions of the fracture surface (thickness w , breadth b , and notch depth a_0) were consulted, in combination with the length l of the cantilever and the maximum force recorded at failure F_f , to derive a value for the critical stress intensity K_{IC} for every cantilever, utilising the following equations outlined in various studies [22,49,50].

$$K_{IC} = \frac{F_f l}{bw^{3/2}} f\left(\frac{a_0}{w}\right), \quad (3)$$

Therein $f(a_0/w)$ represents the following polynomial shape function:

$$f\left(\frac{a_0}{w}\right) = 1.46 + 24.36\left(\frac{a_0}{w}\right) - 47.21\left(\frac{a_0}{w}\right)^2 + 75.18\left(\frac{a_0}{w}\right)^3, \quad (4)$$

The cross-sectional fracture surfaces were analysed, regarding their dimensions and morphology, with an FEI Quanta 250 FEG (a field

emission gun scanning electron microscope – FEGSEM). Structural analyses of the film before and after the heating sequence were performed by X-ray diffraction (XRD), employing a symmetric Bragg-Brentano X-ray diffraction setup. The system was equipped with a Ge (220) hybrid monochromator, which ensured an incident beam of $Cu-K\alpha_1$ radiation only.

A JEOL2100F transmission electron microscope, equipped with an image-side C_s -corrector, was used in this study, which demonstrates a resolution of 1.2 Å at 200 kV. The aberration coefficients were set to be sufficiently small, under which the high resolution transmission electron microscopy (HRTEM) images were taken under slightly over-focused conditions (close to Scherzer defocus). Scanning TEM (STEM) images shown in this paper were recorded using a high-angle annular dark-field (HAADF)/bright-field (BF) detector, with the inner and outer angle of the HAADF detector set to 54 mrad and 144 mrad, respectively, and a BF detector angle of less than 10 mrad.

To investigate the hardness and indentation modulus of the TiN film before and after undergoing the heating procedure, we worked with a Fischer Cripps Laboratories ultra-microindentation system (UMIS) equipped with a Berkovich indenter tip. In total, 31 indentations were performed on the sample in both instances with forces ranging from 3 mN to 45 mN. All indents exceeding a depth of 10% of the coating thickness were excluded from the evaluation, to minimise the influence of the substrate on the final results. We performed the analysis of the recorded data in accordance with the Oliver and Pharr method [51]. The indentation modulus was derived from the reduced modulus recorded by the UMIS system as outlined by Fischer-Cripps [52].

The residual stress state of TiN as function of the temperature was analysed using a kSA MOS Thermal Scan wafer curvature measurement system. The peak temperature of the measurement was set to 773 K, and two different heating rates of 0.5 K/s, and 0.1 K/s, respectively, were used and evaluated. We instructed the system to hold the peak temperature for 2 h before initiating passive vacuum cooling. The temperature- and time-dependent curvature data provided by the instrument was converted into residual stress values using Stoney’s equations in compliance with the guidelines provided by Janssen et al. [53].

To quantify the influence of macro residual stresses in the film on the system fracture toughness of a TiN film on a Si substrate we performed a fracture mechanical analysis. The total stress intensity factor K_{tot} can be defined as the superposition of the stress intensity factor introduced by an external load K_{ext} and by the residual stress state K_{res} .

$$K_{tot} = K_{ext} + K_{res}, \quad (5)$$

If K_{tot} equals or exceeds the material’s inherent fracture toughness K_{IC} the crack will propagate. We define the system fracture toughness K_{sys} as the critical stress intensity factor corresponding to the externally applied load, i.e. the fracture toughness we would experimentally determine for a system with residual stresses. Hence, we can rewrite Eq. 5:

$$K_{sys} = K_{IC} - K_{res}, \quad (6)$$

We assess the contribution of the residual stress state by means of an analytical approach proposed by Beuth [38] for thin bonded films in residual tension. It allows to estimate the stress intensity factor for a partially cracked film on a semi-infinite substrate as a function of crack length a for a given film thickness t with uniform stress in the film. The stress intensity factor associated with the residual stress state σ_{res} is given by

$$K_{res} = \sigma_{res} \sqrt{\pi t} F\left(\alpha, \beta, \frac{a}{t}\right), \quad (7)$$

where $F(\alpha, \beta, a/t)$ is a dimensionless quantity depending on the geometry and the Dundurs parameters (α, β) which describe the elastic mismatch between film and substrate considering plane strain conditions.

The fact that compressive residual stresses would lead to crack closure does not constitute a problem for the herein analysed situation, as we define the total stress intensity factor K_{tot} as the superposition of K_{ext} and K_{res} . Stresses with a negative sign in Eq. 7, corresponding to compressive thermal residual stresses, simply lead to an increase of the system fracture toughness given by Eq. 6.

Lastly, whenever possible, experimental results and measurements in this document are quoted in terms of their sample mean and standard error.

3. Results & discussion

3.1. Theoretical studies

Our theoretical results demonstrate that the surface energies decrease slightly with increasing temperature. As visualised in Fig. 1a, the results from DFT and MD show the same trend for the (100) surface. Although the energies calculated by DFT do not perfectly match those provided by MD, they are of similar magnitude. A certain mismatch is expectable, since it has been demonstrated that the accuracy of surface energies calculated by DFT is rather limited in general [54]. Within the experimentally relevant temperature range from 300 to 800 K, γ_{100} decreases by 1.6%. The MD simulations show a decrease of 4.6% for the (100) surface. For the (110) and (111) surfaces the changes are of smaller magnitude with 1.7 and 1.6%. We note that the error stemming from using harmonic approximation (HA) neglecting thermal expansion is expected to be negligible. In the first instance, we can correct the HA data by including thermal expansion term to the surface area. Considering thermal expansion, the surface energy drop increases from 1.6% to 2.8% over the temperature range 300–800 K. Further improvement would be related to employing (computationally much heavier) quasi-harmonic approximation instead of HA, but this is beyond the scope of the present paper.

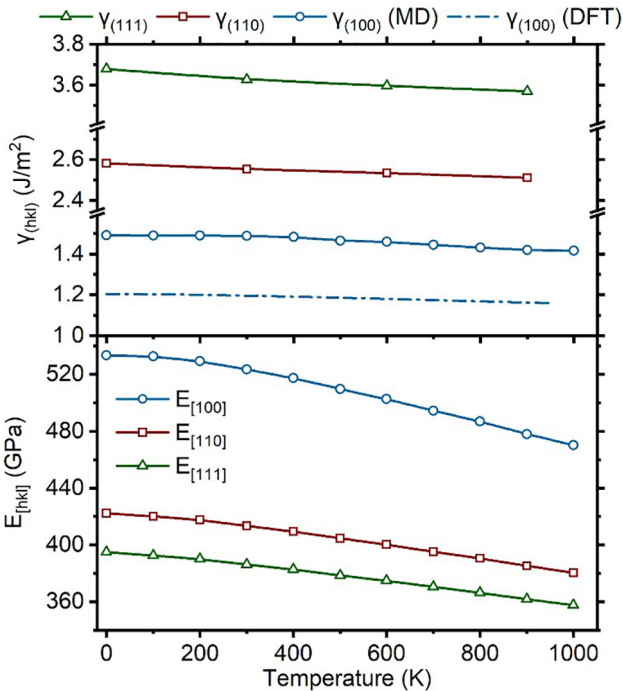


Fig. 1. (100), (110), and (111) surface energies of TiN as a function of temperature (a) calculated using molecular dynamics (MD). The observed trends were verified by calculating a reference for the (100) surface energy via DFT. The temperature-dependence of the directional Young's moduli of TiN (b) were derived from the elastic constants calculated by Shulumba et al.

Shulumba et al. [33] showed that the elastic constants decrease with temperature. As expected, the same holds true for the directional Young's moduli, as illustrated in Fig. 1b. In the aforementioned temperature range, E_{100} decreases by 8.7%. For the [110] and the [111] directions, the Young's moduli decrease by 6.8 and 6.3% respectively. The brittle/ductile behaviour, as predicted by the Pugh [55] and Pettifor [56] criteria, over the same temperature range does not change significantly with a G/B value of 1.5 for the whole range and a Cauchy pressure increase from -30.8 to 28.1 GPa for 273 and 873 K.

Calculating the critical stress intensity K_{IC} over the temperature range predicts a slight decline in the theoretical fracture toughness with a decrease of 6.7, 4.3, and 4.0% for the different surfaces, as depicted in Fig. 2. Deviations of the absolute calculated values of the fracture toughness of TiN (shown in Fig. 2) from experimentally produced ones are to be expected, as ab initio calculations do not consider features, such as growth defects, residual stresses, and grain boundaries, which influence the fracture toughness of an experimentally produced TiN. Also, the TiN films investigated in this study are polycrystalline and measurements performed on them therefore contain influences of all crystallographic directions. In addition to the fact that the fracture mechanism of theory and experiment are not perfectly identical, all of this means that the absolute values in Fig. 2 have to be taken with care. The trends discussed above, however, still provide valuable insight, as they suggest that TiN should have a relatively constant fracture toughness over the studied temperature range – from an atomistic perspective.

3.2. Structural analyses

The XRD patterns of our TiN coating on Si (100) before and after the heating cycle of the fracture toughness testing procedure, depicted in Fig. 3, show a clear fcc peak sequence in both cases and align with the reference pattern for rocksalt (rs) TiN. In both instances, the film shows a diffraction pattern characteristic of a material without any strongly preferred crystalline orientation. Upon completing the heating sequence, the sample displays a slight intensification of the (100) peak. The testing procedure at elevated temperatures also appears to reduce the width of the (111) and (200) peaks. The full width at half maximum (FWHM) of the (111) peak decreases from 0.37° (pre-HT) to 0.34° (post-HT). Analogously, the full width at half maximum of the (200) peak is also narrowed from 0.39° to 0.35° as a consequence of the heat treatment. A small shift to higher diffraction angles, indicative of a decreased d-spacing and lattice parameter, can also be observed for these two peaks as a result of the high temperature treatment with a maximum temperature of 773 K. These two features (reduced FWHM and d-spacing) are established indicators of recovery effects, whereby

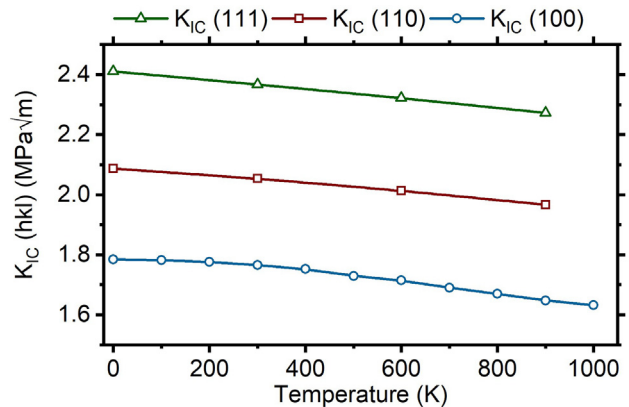


Fig. 2. Theoretically predicted trend of the critical stress intensity as a function of temperature.

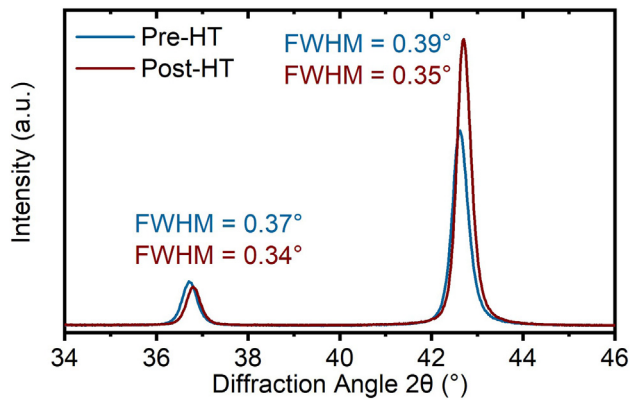


Fig. 3. XRD patterns of the TiN film before and after the high temperature testing procedure. The full width at half maximum (FWHM) is quoted for both the (111) peaks (left) and the (200) peaks (right).

growth-induced structural defects (such as point and line defects) rearrange towards lower-energy sites (sometimes even annihilate) at temperatures above the deposition temperature of 653 K. Please note that changes in the macro residual stress state of the film also affect the d-spacing measured by XRD. Theoretically, grain growth and/or recrystallisation may also cause the observed intensification and narrowing of the Bragg peaks, however, for TMNs, such events are typically reported at temperatures significantly higher than 773 K.

Further information on the (micro-)structural changes occurring within the TiN film during the high temperature testing process can be derived via transmission electron microscopy (TEM). Fig. 4a and b show BF-STEM (bright-field scanning TEM) images of an as-deposited TiN coating (equivalent to pre-HT in Fig. 5a), and of the TiN film after the testing procedure at elevated temperatures (post-HT), respectively. Fig. 4c and d depict accordingly BF-TEM images of the two samples. The untreated sample (Fig. 4a) shows a higher prevalence of dark spots and striations – and thus a higher number of scattering sites for electron – compared to the sample that underwent the heating cycle (Fig. 4b). These features are likely clusters of point and/or line defects, and

therefore the TEM micrographs of the heated sample exhibit a reduced concentration of defects. Due to the annihilation of the darkened features, the columnar grain structure is more clearly visible in the BF-STEM, and BF-TEM images of the “annealed” TiN sample (Fig. 4b, and d, respectively). The grain size and shape appear to remain unaffected by the heating procedure of the high temperature fracture toughness tests, based on our TEM investigations. Close examination of Fig. 4d indicates pore formation at the grain boundaries, as a result of the high temperature testing procedure, due to defect condensation and annihilation at the grain boundaries. High-resolution TEM (HRTEM) images of the untreated (as deposited) TiN film and the heat-treated TiN sample are provided in Fig. 4e and f, respectively. In these presented images, the recovery-related difference is not as apparent as in the BF-STEM, and -TEM micrographs, however in the as-deposited state the TiN exhibits a higher number of blurred, distorted regions, which may be caused by dislocations. The HRTEM micrograph of the heat-treated TiN sample, on the other hand, exhibits a more defect-free crystalline structure.

3.3. Intrinsic fracture toughness of TiN at elevated temperatures

In Fig. 5a we present the intrinsic fracture toughness of polycrystalline TiN (in terms of the critical stress intensity K_{IC}) recorded at 298 (before any post-deposition heating), 473, 673, and 773 K, and again after cooling down to a RT of 296 K. Fig. 5b and c depict SEM micrographs of a representative microcantilever before testing and a typical fracture cross-section of a cantilever after failure, respectively. The initial (as deposited) fracture toughness of our TiN thin film was measured to be 2.9 ± 0.1 MPa \sqrt{m} at a RT of 298 K.

Compared to past studies, our measurement resides at the higher end of the spectrum of fracture toughness values reported for TiN, which typically vary roughly between 2 and 3 MPa \sqrt{m} [23,24,27,57]. This slight elevation of our K_{IC} value compared to other studies may be caused by a combination of multiple different factors originating from the synthesis and testing procedures. Firstly, since our study focuses solely on TiN, we were able to optimise the deposition conditions of the sputtering process for the growth of a TiN film with favourable mechanical properties. Secondly, microcantilever bending tests are

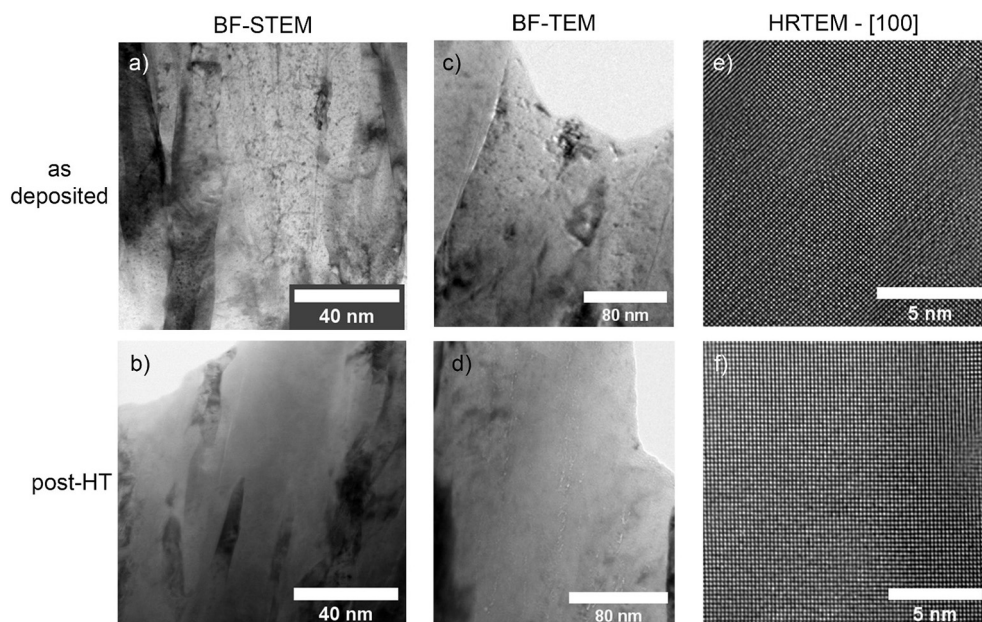


Fig. 4. Bright-field STEM (a and b), bright-field TEM (c and d), and high-resolution TEM (e and f) micrographs of pristine, and heat-treated TiN, respectively. The viewing axis of the HRTEM images is the [100] direction.

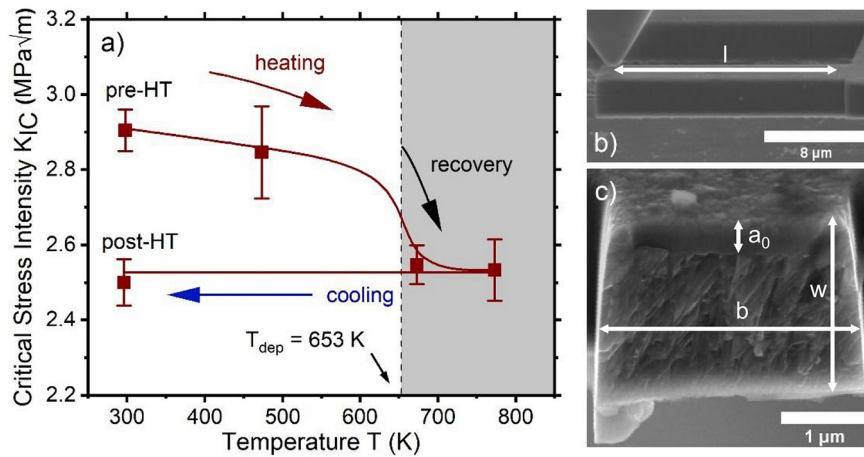


Fig. 5. Plot of the fracture toughness – in terms of the critical stress intensity K_{IC} – versus the testing temperature (a). The effective substrate temperature during the deposition process T_{dep} is highlighted, as well as the room temperature values of K_{IC} before and after the high temperature testing steps. The connecting line was added as guidance in accordance with our interpretation of the data. The SEM micrographs in (b) and (c) show a typical cantilever before and after fracture at room temperature (pre-HT).

known to be sensitive to the notch and bridge geometries [58,59]. We performed our tests in accordance with the findings of Brinckmann et al. [58], who recommend a displacement-controlled setup and bridged notches that exceed an a/w ratio of ~ 0.15 . Nevertheless, given the geometries of our notches and bridges (Fig. 5c), our measurements are more likely to be affected by a small degree of overestimation than by underestimation [58].

Upon increasing the testing temperature from 298 K to 473 K, the critical stress intensity decreases only marginally. This small decrease may reflect the minor reduction of both the surface energy and the Young's modulus observed in the DFT and MD calculations. However, the difference between these two data points is completely covered by the error of both measurements, and may therefore be entirely fictional. The subsequent noticeable decrease of the fracture toughness to 2.6 ± 0.1 MPa√m as the temperature is increased to 673 K can no longer be attributed solely to measurement uncertainties. By completing this heating step, the deposition temperature of 653 K is surpassed, and therefore recovery effects may ensue. A further elevation of the testing temperature to 773 K only results in an additional minor decrease of the critical stress intensity to roughly 2.5 ± 0.1 MPa√m, fully covered by the measurement error, which may be explained by continuing recovery processes. However, measurement errors, local deviations from the measured temperature, and the minor detrimental influence of the temperature on the surface energy, as observed by our theoretical studies, have to be taken into consideration for this last observation. In general, the TiN microcantilevers failed in an intergranular manner, as depicted in Fig. 5c.

As the sample is cooled from 773 K to a RT of 296 K, the fracture toughness remains virtually constant. The observation that the drop in K_{IC} , recorded as soon as the deposition temperature was exceeded, is irreversible by cooling back to RT serves as additional evidence for the impact of recovery effects on the fracture toughness. Moreover, results produced by nanoindentation outline a clear decrease of the hardness from 31.9 ± 0.7 (pre-HT) to 27.3 ± 0.6 GPa (post-HT). The indentation modulus remains relatively constant at 481.8 ± 6.8 and 475.0 ± 11.0 GPa respectively. It has to be noted that – unlike the microcantilever bending tests – nanoindentation is influenced by changes of the residual stress state of the film. However, a decreasing hardness is a common observation associated with the recovery of growth defects [23,60,61]. Hence, in combination with the structural investigations of the previous sections, the nanoindentation results suggest as well that neither the temperature dependence of the elastic constants, nor the surface energies are responsible for the significant

decrease in K_{IC} , but the associated recovery effects when surpassing the deposition temperature.

The load-deflection curves of all cantilevers depicted in Fig. 6a present a similar spread of the data for all measurement temperatures. This suggests that most of the deviation in apparent stiffness supposedly observable in Fig. 6a actually originates from geometrical differences between the cantilevers. Particularly representative cantilevers for each temperature are displayed opaquely in Fig. 6a and represented in Fig. 6b in terms of stress intensity and relative deflection. For the latter quantity, the absolute deflection at each point of the load cycle was divided by the thickness of the cantilever in question, as all other dimensions were chosen in relation to the thickness. This normalised set of data further reinforces the impression that the apparent stiffness of the cantilevers remains essentially constant across the investigated temperature range. Contrastingly, the maximum stress intensity, as well as the relative elastic deformation limit are both reduced noticeably by the heating procedure. This indicates that the energy absorbed upon fracture of TiN is also decreased by thermally induced recovery.

The results of all toughness-related investigations further imply that no brittle-to-ductile transition, nor any other thermally activated change of the fracture mechanism itself, occurs up to 773 K. Furthermore, based on the results of the present study, the influence of the temperature (over the examined range) on the bonding characteristics appears to be rather small, barely manifesting in a measurable change of the critical stress intensity and/or apparent stiffness. Our results unanimously implicate recovery of point and line defects in the drop of the fracture toughness with increasing temperatures. Thermally induced recovery effects have been investigated by past studies, which reported a decrease in the magnitude of micro-strains [62,63], hardness [60,61], and dislocation density [63], as well as a significant reduction of the electrical resistivity of TiN thin films [64,65]. Both point and line defects, and the associated microstrains, are known to be prominent features in PVD-produced thin films [62]. Our evidence thus suggests that the presence of point-defect- and dislocation-induced microstrains has a positive effect on the fracture toughness of TiN thin films. Furthermore, the results of the present study demonstrate that temperatures up to 773 K do not have a significant adverse effect on the fracture toughness of TiN coatings.

By depicting an overall drop of the fracture toughness with increasing temperature up to 773 K, our results for TiN show a contrasting trend to those reported by Best et al. for nanolayered coatings [31], who found increasing K_{IC} values with increasing temperature. The rather complex nanolayered coatings (containing also metastable cubic AlN) investigated in their study impedes a straightforward

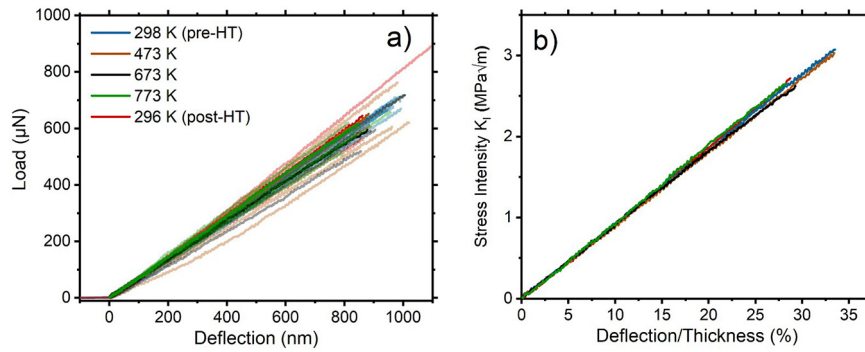


Fig. 6. Load-Deflection plots of all TiN microcantilevers tested in this study (a). Particularly representative cantilevers for each temperature increment are shown opaquely in (a) and plotted in (b) in terms of stress intensity and deflection in relation to their respective thickness.

comparison with our results found for monolithic TiN. For pure monolithic CrN, Best et al. noted a limited accuracy of the pillar splitting approach used in their study (they observed a combination of deformation modes, including deformation of the outer pillar circumference). Another potential origin of the divergent observed trends might be the lower decomposition and melting temperature of CrN compared to TiN [66,67]. Thus, the experiments on CrN were effectively conducted within a significantly higher region of the homologous temperature than those on TiN of the present study. In a different study, Ga ion embrittlement – a concept traditionally associated with metallic materials [68] – was seen to occur in FIB-notched CrN microcantilevers at elevated temperatures [30]. The reason for this conclusion was that their measured fracture toughness remained unchanged by heating to 773 K and decreased significantly upon cooling back to RT. However, definitive proof was not provided. This trend does not align with that recorded by our experiments, since we observe a noticeable decrease of the fracture toughness already upon heating beyond the deposition temperature, and virtually no change as a result of cooling back to RT. If thermally activated Ga ion diffusion were to embrittle our sample, we would therefore expect to see a significant decrease in fracture toughness upon cooling [30,69]. Therefore, it seems that our TiN sample was not significantly embrittled by Ga ion diffusion. Furthermore, other studies performing microcantilever bending tests on non-metallic materials have not provided evidence for Ga ion embrittlement. In situ investigations of Si microcantilevers at elevated temperatures, for instance, have not shown the effect [8]. Our results match those of Riedl, Daniel et al. [70], who cut microcantilevers into as-deposited and annealed samples of CrN, which were then tested at RT. They demonstrated that annealing above the deposition temperature leads to a measurable reduction of the fracture toughness, for which they also cite growth defect recovery – and the associated relaxation of compressive micro residual stresses – as a likely explanation [70]. The fact that the cantilevers of their study were cut after the samples had been annealed eliminates Ga ion embrittlement as a possible origin of the temperature-related decrease of the fracture toughness in CrN for their study.

3.4. Apparent system fracture toughness of TiN on Si at elevated temperatures

In the previous section, we explored the intrinsic fracture toughness of TiN without the influence of residual stresses. As long as a TiN film is supported by a substrate, however, which is the reality in most applications of the material, residual stresses affect its mechanical properties. In this section, we therefore aim to provide a methodological example of how the intrinsic fracture toughness values may be combined with the temperature-dependent residual stress state of TiN on a given substrate to extract the system fracture toughness of a TiN film on that given substrate at different temperatures. In Fig. 7a we present the

residual stress state of a 2.8 µm TiN film on a Si (100) wafer as a function of temperature. As outlined in the section covering the experimental methodology, we measured the curvature of the wafer and converted the readings into residual stress data via Stoney's Eq. [53]. According to these results, the untreated, as deposited, TiN film possesses roughly –1.1 GPa of compressive residual stresses. We conducted the experiments for two different heating rates of 0.1 and 0.5 K/s. In each instance, the peak temperature was set to 773 K.

For each heating rate, the temperature increase causes an intensification of the compressive residual stresses, as the Si (100) substrate impedes the thermal expansion of the TiN films. The peak temperature was kept constant for 2 h in each case, and Fig. 7b and c show that the curvature changes logarithmically over that period. This serves as an additional piece of evidence of growth defect recovery, as the logarithmic time-dependence at a constant temperature suggests the occurrence of a thermally activated, diffusive process. The lower heating rate of 0.1 K/s is also capable of resolving the onset of this process below the peak temperature. During cool-down, the thermal stresses of the heating procedure are relieved, leading to the characteristic hysteresis depicted in Fig. 7a. The observation that defect recovery causes relaxation of compressive residual stresses in the film aligns with the reduction in d-spacing recorded by XRD (Fig. 3). A less compressive residual stress state allows for an elongation of the interplanar spacings parallel to the substrate-film interface, which is compensated by a shortening of the d-spacings normal to the interface (measured by XRD). Combining these residual stress measurements (Fig. 7) with the TEM investigations (Fig. 4) therefore suggests that growth defect recovery lowers the intrinsic fracture toughness of TiN by causing the formation of pores at the grain boundaries, and reducing the microstrains in the film.

In theory, grain growth would cause a similar curvature-temperature profile, however, in the past it has been shown that grain growth in TiN-based materials becomes significant at temperatures considerably higher than those studied in the present investigations [60,71,72]. For CrN, Daniel et al. [73] have reported grain growth to occur at a significant rate at 1173 K. Mayrhofer et al. [67] have detected the onset of recrystallisation-related grain growth in CrN at about 1073 K. Moreover, our morphological investigations did not indicate any significant changes of size and shape of the columnar grains, and TiN is considered to possess a higher thermal stability than CrN, which has been demonstrated to release nitrogen and decompose into Cr₂N at about 1273 K [60,67,74]. Therefore, grain growth and/or recrystallisation does not seem to be a relevant factor in our study.

Using the weight function approach outlined in the methodology section, we combine the temperature-dependent intrinsic fracture toughness of TiN captured by the microcantilever bending tests with residual stress measurements of TiN on Si at each temperature (analogous to Fig. 7) to estimate the impact of elevated temperatures on the overall system fracture toughness of our TiN film on Si (100). The residual stress of each data point was measured by heating to the

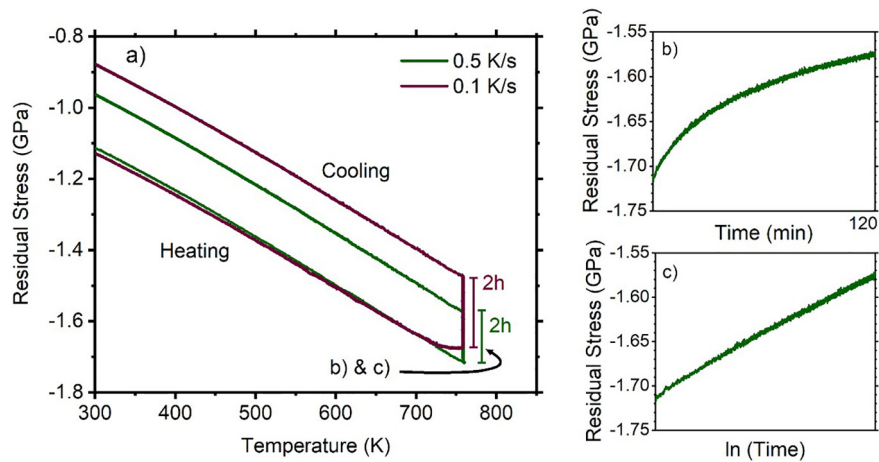


Fig. 7. Plot of the residual stress state as function of temperature for two different heating rates (a). The 2 h holding period of the peak temperature of 773 K shows a logarithmic change of the residual stresses over time (b and c).

respective peak temperature at a rate of 0.5 K/s, and holding this temperature for 2 h to allow for any potential recovery effects to progress sufficiently.

As an example for the effect of residual stresses within the realistic configuration of a thin film attached to a semi-infinite substrate, we present the system fracture toughness values gained by the analytical model for an initial crack with an a/t ratio of 0.2, where a refers to the initial crack length and t to the film thickness ($2.8 \mu\text{m}$). Fig. 8 depicts the results of this continuum mechanics (CM)-based model in comparison with the experimentally recorded intrinsic fracture toughness readings of Fig. 5a, where the macrostresses are fully relaxed. The results therein show that the compressive residual stresses imposed by the substrate, which intensify upon heating, elevate the expected critical stress intensity of the TiN-Si system as the temperature is increased. A decrease of K_{IC} is only noticeable upon heating from 673 K to 773 K. Still, the system fracture toughness of TiN-Si at 773 K ($5.2 \text{ MPa}\sqrt{\text{m}}$)

exceeds that of as-deposited TiN-Si ($4.6 \text{ MPa}\sqrt{\text{m}}$). Upon cooling back to RT, the recovery-related decrease in toughness becomes apparent also in the TiN-Si system. In relative terms, the system K_{IC} is reduced by 14% from $4.6 \text{ MPa}\sqrt{\text{m}}$ (pre-HT) to $4.0 \text{ MPa}\sqrt{\text{m}}$ (post-HT) as a result of the heating procedure and its associated events. This relative decrease of the system fracture toughness is effectively identical to that of the intrinsic fracture toughness from $2.9 \text{ MPa}\sqrt{\text{m}}$ to $2.5 \text{ MPa}\sqrt{\text{m}}$. Overall, our analytical estimations demonstrate that the residual stress state presents a vital contribution to the TiN-Si system fracture toughness. For other TiN films attached to different substrates, this model would yield noticeably different results. Thus, for temperatures up to 773 K our investigations show that the fracture behaviour of TiN on any given substrate, just like at RT, is primarily governed by the film-substrate relationship, as well as the thermal and processing history of the material.

4. Summary & conclusions

We have examined the fracture-related properties of TiN thin films from an experimental and computational viewpoint. Providing the theoretical foundation for this study, we used molecular dynamics to calculate the (100), (110), and (111) surface energies of TiN and show that they only decrease marginally as the temperature is increased from 0 to 1000 K. In the experimentally relevant temperature range from 298 K (25°C) to 773 K (500°C), the change is particularly insignificant. We also calculated the (100) surface energies via DFT to verify the trends observed in our MD simulations. By combining our results for the surface energies with existing data for the elastic constants of TiN at elevated temperatures, we predicted a relatively constant development of the critical stress intensity K_{IC} across both the theoretical and experimental temperature span.

The results of our micromechanical single-cantilever bending tests conducted in situ at the elevated temperatures mentioned above recorded no significant direct influence of the temperature on K_{IC} up to 773 K (500°C), thereby mirroring the observed theoretical trends. A noteworthy change occurred only once the deposition temperature of the TiN film had been surpassed, which led to a decrease of the fracture toughness from 2.9 ± 0.1 to $2.5 \pm 0.1 \text{ MPa}\sqrt{\text{m}}$. As this was unrecoverable upon cooling the TiN film back down to room temperature, we identified thermally induced solid state reactions, i.e. recovery of growth defects above the deposition temperature as the main driving force behind this drop. The occurrence of recovery is further evidenced by a drop in hardness from 31.9 ± 0.7 (before the heating sequence) to $27.3 \pm 0.6 \text{ GPa}$ (after the heating sequence), as well as structural

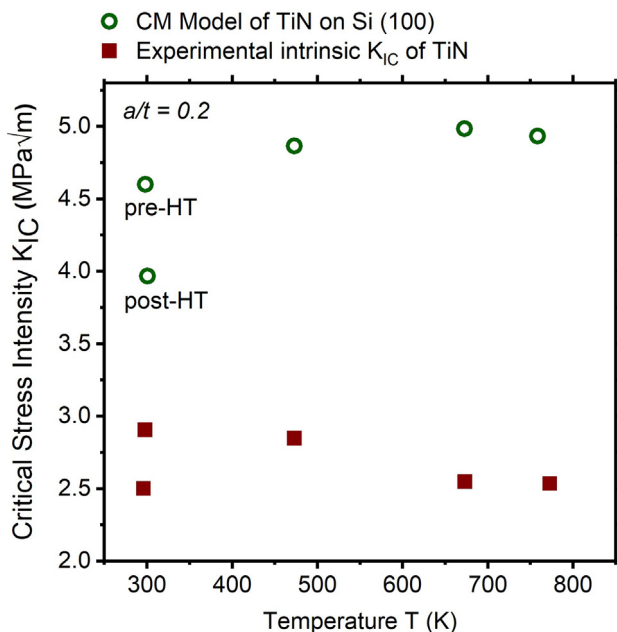


Fig. 8. Critical stress intensity of TiN attached to a Si (100) substrate as a function of temperature based on the continuum mechanics (CM) model. The experimental values of the intrinsic (residual-stress-free) fracture toughness of Fig. 5a are added to act as comparison.

changes uncovered by TEM micrographs and XRD patterns recorded before and after the heating cycle.

The recorded load-deflection curves further demonstrate the beneficial effect of growth-induced defects (such as dislocations and point defects) on the toughness-related properties of TiN, as the critical stress intensity is reduced virtually in unison with the relative deformability of the TiN cantilevers.

Lastly, we performed wafer curvature measurements of TiN films on Si (100) substrates at temperature ranging from RT to 773 K, which we used to calculate the temperature-dependent residual stress state of the TiN films. Holding the peak temperature for 2 h revealed the occurrence of a time-dependent diffusive process above the deposition temperature, thus also hinting at growth defect recovery. Using an analytical method, we combine the residual stress state of TiN with the intrinsic – residual stress free – fracture toughness of TiN at every available temperature to estimate the effective system fracture toughness of TiN attached to a Si (100) substrate at each temperature. These calculations reveal that residual stresses govern the fracture properties of TiN at elevated temperatures, while the change in inherent fracture toughness is comparably small.

Acknowledgement

JB, LL, AW, DH, and MB highly acknowledge the financial support of the Austrian Science Fund (FWF): P30341-N36. The computational results presented have been achieved using the Vienna Scientific Cluster (VSC). The authors acknowledge the use of the facilities of USTEM and XRC at TU Wien.

Data availability

The raw/processed data required to reproduce these findings cannot be shared at this time as the data also forms part of an ongoing study.

Declaration of Competing Interest

The authors declare that they have no known competing financial interests or personal relationships that could have appeared to influence the work reported in this paper.

References

- [1] M.E. Launey, R.O. Ritchie, On the fracture toughness of advanced materials, *Adv. Mater.* 21 (2009) 2103–2110, <https://doi.org/10.1002/adma.200803322>.
- [2] R.O. Ritchie, Mechanisms of fatigue crack propagation in metals, ceramics and composites: role of crack tip shielding, *Mater. Sci. Eng. A* 103 (1988) 15–28, [https://doi.org/10.1016/0025-5416\(88\)90547-2](https://doi.org/10.1016/0025-5416(88)90547-2).
- [3] R.O. Ritchie, The conflicts between strength and toughness, *Nat. Mater.* 10 (2011) 817–822, <https://doi.org/10.1038/nmat3115>.
- [4] A.G. Evans, Perspective on the development of high-toughness ceramics, *J. Am. Ceram. Soc.* 73 (1990) 187–206, <https://doi.org/10.1111/j.1151-2916.1990.tb06493.x>.
- [5] D. Raut, R.L. Narayan, P. Tandaiya, U. Ramamurty, Temperature-dependence of mode I fracture toughness of a bulk metallic glass, *Acta Mater.* 144 (2018) 325–336, <https://doi.org/10.1016/j.actamat.2017.10.063>.
- [6] K. Samuel, O. Gossmann, H. Huthmann, Temperature dependence of fracture toughness (J–R-curves) of a modified type 316L austenitic stainless steel, *Int. J. Press. Vessel. Pip.* 41 (1990) 59–74, [https://doi.org/10.1016/0308-0161\(90\)90077-U](https://doi.org/10.1016/0308-0161(90)90077-U).
- [7] D. Lassance, D. Fabrègue, F. Delannay, T. Pardoen, Micromechanics of room and high temperature fracture in 6xxx Al alloys, *Prog. Mater. Sci.* 52 (2007) 62–129, <https://doi.org/10.1016/j.pmatsci.2006.06.001>.
- [8] B.N. Jaya, J.M. Wheeler, J. Wehrs, J.P. Best, R. Soler, J. Michler, C. Kirchlechner, G. Dehm, Microscale fracture behavior of single crystal silicon beams at elevated temperatures, *Nano Lett.* 16 (2016) 7597–7603, <https://doi.org/10.1021/acs.nanolett.6b03461>.
- [9] J. Ast, J.J. Schwiedrzik, J. Wehrs, D. Frey, M.N. Polyakov, J. Michler, X. Maeder, The brittle-ductile transition of tungsten single crystals at the micro-scale, *Mater. Des.* 152 (2018) 168–180, <https://doi.org/10.1016/j.matdes.2018.04.009>.
- [10] A. Achour, R.L. Porto, M.-A. Soussou, M. Islam, M. Boujtita, K.A. Aissa, L. Le Brizoual, A. Djouadi, T. Brousse, Titanium nitride films for micro-supercapacitors: effect of surface chemistry and film morphology on the capacitance, *J. Power Sources* 300 (2015) 525–532, <https://doi.org/10.1016/j.jpowsour.2015.09.012>.
- [11] H.G. Leduc, B. Bumble, P.K. Day, B.H. Eom, J. Gao, S. Golwala, B.A. Mazin, S. McHugh, A. Merrill, D.C. Moore, O. Noroozian, A.D. Turner, J. Zmuidzinas, Titanium nitride films for ultrasensitive microresonator detectors, *Appl. Phys. Lett.* 97 (2010), 102509, <https://doi.org/10.1063/1.3480420>.
- [12] L. Gui, S. Bagheri, N. Strohfeldt, M. Hentschel, C.M. Zgrabik, B. Metzger, H. Linnenbank, E.L. Hu, H. Giessen, Nonlinear refractory plasmonics with titanium nitride nanoantennas, *Nano Lett.* 16 (2016) 5708–5713, <https://doi.org/10.1021/acs.nanolett.6b02376>.
- [13] B.G. Kim, C. Jo, J. Shin, Y. Mun, J. Lee, J.W. Choi, Ordered mesoporous titanium nitride as a promising carbon-free cathode for aprotic lithium-oxygen batteries, *ACS Nano* 11 (2017) 1736–1746, <https://doi.org/10.1021/acsnano.6b07635>.
- [14] B. Avsarala, P. Haldar, Durability and degradation mechanism of titanium nitride based electrocatalysts for PEM (proton exchange membrane) fuel cell applications, *Energy* 57 (2013) 545–553, <https://doi.org/10.1016/j.energy.2013.05.021>.
- [15] E. Santecchia, A.M.S. Hamouda, F. Musharavati, E. Zalnezhad, M. Cabibbo, S. Spigarelli, Wear resistance investigation of titanium nitride-based coatings, *Ceram. Int.* 41 (2015) 10349–10379, <https://doi.org/10.1016/j.ceramint.2015.04.152>.
- [16] G. Abadias, Stress and preferred orientation in nitride-based PVD coatings, *Surf. Coat. Technol.* 202 (2008) 2223–2235, <https://doi.org/10.1016/j.surfcoat.2007.08.029>.
- [17] C. Kral, W. Lengauer, D. Rafaja, P. Ettmayer, Critical review on the elastic properties of transition metal carbides, nitrides and carbonitrides, *J. Alloys Compd.* 265 (1998) 215–233, [https://doi.org/10.1016/S0925-8388\(97\)00297-1](https://doi.org/10.1016/S0925-8388(97)00297-1).
- [18] J. Ast, M. Ghidelli, K. Durst, M. Göken, M. Sebastiani, A.M. Korsunsky, A review of experimental approaches to fracture toughness evaluation at the micro-scale, *Mater. Des.* 173 (2019), 107762, <https://doi.org/10.1016/j.matdes.2019.107762>.
- [19] G. Dehm, B.N. Jaya, R. Raghavan, C. Kirchlechner, Overview on micro- and nanomechanical testing: new insights in interface plasticity and fracture at small length scales, *Acta Mater.* 142 (2018) 248–282, <https://doi.org/10.1016/j.actamat.2017.06.019>.
- [20] T. Chudoba, P. Schwaller, R. Rabe, J.-M. Breguet, J. Michler, Comparison of nanoindentation results obtained with Berkovich and cube-corner indenters, *Philos. Mag.* 86 (2006) 5265–5283, <https://doi.org/10.1080/14786430600746424>.
- [21] M. Sebastiani, K.E. Johanns, E.G. Herbert, F. Carassiti, G.M. Pharr, A novel pillar indentation splitting test for measuring fracture toughness of thin ceramic coatings, *Philos. Mag.* 95 (2015) 1928–1944, <https://doi.org/10.1080/14786435.2014.913110>.
- [22] K. Matoy, H. Schönherr, T. Detzel, T. Schöberl, R. Pippan, C. Motz, G. Dehm, A comparative micro-cantilever study of the mechanical behavior of silicon based passivation films, *Thin Solid Films* 518 (2009) 247–256, <https://doi.org/10.1016/j.tsf.2009.07.143>.
- [23] M. Bartosik, C. Rumeau, R. Hahn, Z.L. Zhang, P.H. Mayrhofer, Fracture toughness and structural evolution in the TiAlN system upon annealing, *Sci. Rep.* 7 (2017), 16476, <https://doi.org/10.1038/s41598-017-16751-1>.
- [24] S. Massl, W. Thomma, J. Keckes, R. Pippan, Investigation of fracture properties of magnetron-sputtered TiN films by means of a FIB-based cantilever bending technique, *Acta Mater.* 57 (2009) 1768–1776, <https://doi.org/10.1016/j.actamat.2008.12.018>.
- [25] M. Bartosik, R. Hahn, Z.L. Zhang, I. Ivanov, M. Arndt, P. Polcik, P.H. Mayrhofer, Fracture toughness of Ti-Si-N thin films, *Int. J. Refract. Met. Hard Mater.* 72 (2018) 78–82, <https://doi.org/10.1016/j.jrmm.2017.12.015>.
- [26] R. Hahn, M. Bartosik, R. Soler, C. Kirchlechner, G. Dehm, P.H. Mayrhofer, Superlattice effect for enhanced fracture toughness of hard coatings, *Scr. Mater.* 124 (2016) 67–70, <https://doi.org/10.1016/j.scriptamat.2016.06.030>.
- [27] J. Buchinger, N. Koutná, Z. Chen, Z. Zhang, P.H. Mayrhofer, D. Holec, M. Bartosik, Toughness enhancement in TiN/WN superlattice thin films, *Acta Mater.* 172 (2019) 18–29, <https://doi.org/10.1016/j.actamat.2019.04.028>.
- [28] R. Hahn, M. Bartosik, M. Arndt, P. Polcik, P.H. Mayrhofer, Annealing effect on the fracture toughness of CrN/TiN superlattices, *Int. J. Refract. Met. Hard Mater.* 71 (2018) 352–356, <https://doi.org/10.1016/j.jrmm.2017.11.008>.
- [29] C.M. Lauener, L. Petho, M. Chen, Y. Xiao, J. Michler, J.M. Wheeler, Fracture of silicon: influence of rate, positioning accuracy, FIB machining, and elevated temperatures on toughness measured by pillar indentation splitting, *Mater. Des.* 142 (2018) 340–349, <https://doi.org/10.1016/j.matdes.2018.01.015>.
- [30] J.P. Best, J. Zechner, J.M. Wheeler, R. Schoepner, M. Morstein, J. Michler, Small-scale fracture toughness of ceramic thin films: the effects of specimen geometry, ion beam notching and high temperature on chromium nitride toughness evaluation, *Philos. Mag.* 96 (2016) 3552–3569, <https://doi.org/10.1080/14786435.2016.1223891>.
- [31] J.P. Best, J. Wehrs, M. Polyakov, M. Morstein, J. Michler, High temperature fracture toughness of ceramic coatings evaluated using micro-pillar splitting, *Scr. Mater.* 162 (2019) 190–194, <https://doi.org/10.1016/j.scriptamat.2018.11.013>.
- [32] P. Steneteg, O. Hellman, O.Y. Vekilova, N. Shulumba, F. Tasnádi, I.A. Abrikosov, Temperature dependence of TiN elastic constants from *ab initio* molecular dynamics simulations, *Phys. Rev. B* 87 (2013), 094114, <https://doi.org/10.1103/PhysRevB.87.094114>.
- [33] N. Shulumba, O. Hellman, L. Rogström, R. Zaza, F. Tasnádi, I.A. Abrikosov, M. Odén, Temperature-dependent elastic properties of Ti_{1-x}Al_xN alloys, *Appl. Phys. Lett.* 107 (2015), 231901, <https://doi.org/10.1063/1.4936896>.
- [34] D.G. Sangiovanni, D. Edström, L. Hultman, I. Petrov, J.E. Greene, V. Chirita, *Ab initio* and classical molecular dynamics simulations of N₂ desorption from TiN(001) surfaces, *Surf. Sci.* 624 (2014) 25–31, <https://doi.org/10.1016/j.susc.2014.01.007>.
- [35] D.G. Sangiovanni, D. Edström, L. Hultman, V. Chirita, I. Petrov, J.E. Greene, Dynamics of Ti, N, and TiN x (x = 1 – 3) ad molecule transport on TiN(001) surfaces, *Phys. Rev. B* 86 (2012), 155443, <https://doi.org/10.1103/PhysRevB.86.155443>.

- [36] D.G. Sangiovanni, Inherent toughness and fracture mechanisms of refractory transition-metal nitrides via density-functional molecular dynamics, *Acta Mater.* 151 (2018) 11–20, <https://doi.org/10.1016/j.actamat.2018.03.038>.
- [37] D.G. Sangiovanni, F. Tasnadi, L.J.S. Johnson, M. Oden, I.A. Abrikosov, Strength, transformation toughening and fracture dynamics of rocksalt-structure Ti1-xAlxN (0 <= x <= 0.75) alloys, *Phys. Rev. Mater.* 4 (2019) <https://doi.org/10.1103/PhysRevMaterials.4.033605>.
- [38] J.L. Beuth, Cracking of thin bonded films in residual tension, *Int. J. Solids Struct.* 29 (1992) 1657–1675, [https://doi.org/10.1016/0020-7683\(92\)90015-L](https://doi.org/10.1016/0020-7683(92)90015-L).
- [39] S. Plimpton, Fast parallel algorithms for short-range molecular dynamics, *J. Comput. Phys.* 117 (1995) 1–19, <https://doi.org/10.1006/jcph.1995.1039>.
- [40] P.E. Blöchl, Projector augmented-wave method, *Phys. Rev. B* 50 (1994) 17953–17979, <https://doi.org/10.1103/PhysRevB.50.17953>.
- [41] G. Kresse, J. Furthmüller, Efficient iterative schemes for ab initio total-energy calculations using a plane-wave basis set, *Phys. Rev. B* 54 (1996) 11169–11186, <https://doi.org/10.1103/PhysRevB.54.11169>.
- [42] G. Kresse, D. Joubert, From ultrasoft pseudopotentials to the projector augmented-wave method, *Phys. Rev. B* 59 (1999) 1758–1775, <https://doi.org/10.1103/PhysRevB.59.1758>.
- [43] A. Togo, I. Tanaka, First principles phonon calculations in materials science, *Scr. Mater.* 108 (2015) 1–5, <https://doi.org/10.1016/j.scriptamat.2015.07.021>.
- [44] M. Ohring, *Materials Science of Thin Films*, Elsevier, 1992 <https://doi.org/10.1016/B978-0-12-524975-1.X5000-9>.
- [45] K. Chen, M. Bielawski, Interfacial fracture toughness of transition metal nitrides, *Surf. Coat. Technol.* 203 (2008) 598–601, <https://doi.org/10.1016/j.surfcoat.2008.05.040>.
- [46] H. Riedl, C.M. Koller, F. Munnik, H. Hutter, F. Mendez Martin, R. Rachbauer, S. Kolozsvári, M. Bartosik, P.H. Mayrhofer, Influence of oxygen impurities on growth morphology, structure and mechanical properties of Ti-Al-N thin films, *Thin Solid Films* 603 (2016) 39–49, <https://doi.org/10.1016/j.tsf.2016.01.039>.
- [47] A. Kirnbauer, A. Kretschmer, C.M. Koller, T. Wojcik, V. Paneta, M. Hans, J.M. Schneider, P. Polcik, P.H. Mayrhofer, Mechanical properties and thermal stability of reactively sputtered multi-principal-metal Hf-Ta-Ti-V-Zr nitrides, *Surf. Coat. Technol.* 389 (2020), 125674, <https://doi.org/10.1016/j.surfcoat.2020.125674>.
- [48] J.M. Wheeler, P. Brodard, J. Michler, Elevated temperature, *in situ* indentation with calibrated contact temperatures, *Philos. Mag.* 92 (2012) 3128–3141, <https://doi.org/10.1080/14786435.2012.674647>.
- [49] D. Di Maio, S.G. Roberts, Measuring fracture toughness of coatings using focused-ion-beam-machined microbeams, *J. Mater. Res.* 20 (2005) 299–302, <https://doi.org/10.1557/JMR.2005.0048>.
- [50] C.E. Athanasiou, H. Zhang, C. Ramirez, J. Xi, T. Baba, X. Wang, W. Zhang, N.P. Padture, I. Szlufarska, B.W. Sheldon, High toughness carbon-nanotube-reinforced ceramics via ion-beam engineering of interfaces, *Carbon N. Y* 163 (2020) 169–177, <https://doi.org/10.1016/j.carbon.2020.02.075>.
- [51] W.C. Oliver, G.M. Pharr, An improved technique for determining hardness and elastic modulus using load and displacement sensing indentation experiments, *J. Mater. Res.* 7 (1992) 1564–1583, <https://doi.org/10.1557/JMR.1992.1564>.
- [52] A.C. Fischer-Cripps, Critical review of analysis and interpretation of nanoindentation test data, *Surf. Coat. Technol.* 200 (2006) 4153–4165, <https://doi.org/10.1016/j.surfcoat.2005.03.018>.
- [53] G.C.A.M. Janssen, M.M. Abdalla, F. van Keulen, B.R. Pujada, B. van Venrooy, Celebrating the 100th anniversary of the Stoney equation for film stress: developments from polycrystalline steel strips to single crystal silicon wafers, *Thin Solid Films* 517 (2009) 1858–1867, <https://doi.org/10.1016/j.tsf.2008.07.014>.
- [54] L. Schimka, J. Harl, A. Stroppa, A. Grüneis, M. Marsman, F. Mittendorfer, G. Kresse, Accurate surface and adsorption energies from many-body perturbation theory, *Nat. Mater.* 9 (2010) 741–744, <https://doi.org/10.1038/nmat2806>.
- [55] S.F. Pugh XCII. Relations between the elastic moduli and the plastic properties of polycrystalline pure metals, London, Edinburgh, Dublin *Philos. Mag. J. Sci.* 45 (1954) 823–843, <https://doi.org/10.1080/14786440808520496>.
- [56] D.G. Pettifor, Theoretical predictions of structure and related properties of intermetallics, *Mater. Sci. Technol.* 8 (1992) 345–349, <https://doi.org/10.1179/mst.1992.8.4.345>.
- [57] M. Ghidelli, M. Sebastiani, K.E. Johanns, G.M. Pharr, Effects of indenter angle on micro-scale fracture toughness measurement by pillar splitting, *J. Am. Ceram. Soc.* 100 (2017) 5731–5738, <https://doi.org/10.1111/jace.15093>.
- [58] S. Brinckmann, K. Matoy, C. Kirchlechner, G. Dehm, On the influence of microcantilever pre-crack geometries on the apparent fracture toughness of brittle materials, *Acta Mater.* 136 (2017) 281–287, <https://doi.org/10.1016/j.actamat.2017.07.014>.
- [59] F. Iqbal, J. Ast, M. Göken, K. Durst, In situ micro-cantilever tests to study fracture properties of NiAl single crystals, *Acta Mater.* 60 (2012) 1193–1200, <https://doi.org/10.1016/j.actamat.2011.10.060>.
- [60] L. Hultman, Thermal stability of nitride thin films, *Vacuum* 57 (2000) 1–30, [https://doi.org/10.1016/S0042-207X\(00\)00143-3](https://doi.org/10.1016/S0042-207X(00)00143-3).
- [61] P. Mayrhofer, F. Kunc, J. Musil, C. Mitterer, A comparative study on reactive and non-reactive unbalanced magnetron sputter deposition of TiN coatings, *Thin Solid Films* 415 (2002) 151–159, [https://doi.org/10.1016/S0040-6090\(02\)00511-4](https://doi.org/10.1016/S0040-6090(02)00511-4).
- [62] M. Bartosik, D. Holec, D. Apel, M. Klaus, C. Genzel, J. Keckes, M. Arndt, P. Polcik, C.M. Koller, P.H. Mayrhofer, Thermal expansion of Ti-Al-N and Cr-Al-N coatings, *Scr. Mater.* 127 (2017) 182–185, <https://doi.org/10.1016/j.scriptamat.2016.09.022>.
- [63] A. Kavitha, R. Kannan, P. Sreedhara Reddy, S. Rajashabala, The effect of annealing on the structural, optical and electrical properties of titanium nitride (TiN) thin films prepared by DC magnetron sputtering with supported discharge, *J. Mater. Sci. Mater. Electron.* 27 (2016) 10427–10434, <https://doi.org/10.1007/s10854-016-5130-0>.
- [64] B.T. Kearney, B. Jugdersuren, J.C. Culbertson, P.A. Desario, X. Liu, Substrate and annealing temperature dependent electrical resistivity of sputtered titanium nitride thin films, *Thin Solid Films* 661 (2018) 78–83, <https://doi.org/10.1016/j.tsf.2018.07.001>.
- [65] N.K. Ponom, D.J.R. Appleby, E. Arac, P.J. King, S. Ganti, K.S.K. Kwa, A. O'Neill, Effect of deposition conditions and post deposition anneal on reactively sputtered titanium nitride thin films, *Thin Solid Films* 578 (2015) 31–37, <https://doi.org/10.1016/j.tsf.2015.02.009>.
- [66] N.N. Greenwood, A. Earnshaw, *Chemistry of the Elements*, Pergamon Press, 1984 p. 1542.
- [67] P.H. Mayrhofer, F. Rovere, M. Moser, C. Strondl, R. Tietema, Thermally induced transitions of CrN thin films, *Scr. Mater.* 57 (2007) 249–252, <https://doi.org/10.1016/j.scriptamat.2007.03.058>.
- [68] M.H. Kamdar, Liquid metal embrittlement, *Treatise Mater. Sci. Technol.* 25 (1983) 361–459, <https://doi.org/10.1016/b978-1-78548-309-7.50022-3>.
- [69] F.E. Wang, *Mechanical properties, Bond. Theory Met. Alloy*, Elsevier 2019, pp. 157–191, <https://doi.org/10.1016/b978-0-444-64201-1.00006-3>.
- [70] A. Riedl, R. Daniel, M. Stefanelli, T. Schöberl, O. Kolednik, C. Mitterer, J. Keckes, A novel approach for determining fracture toughness of hard coatings on the micrometer scale, *Scr. Mater.* 67 (2012) 708–711, <https://doi.org/10.1016/j.scriptamat.2012.06.034>.
- [71] R.A. Andrievski, I.A. Anisimova, V.P. Anisimov, Structure and microhardness of TiN compositional and alloyed films, *Thin Solid Films* 205 (1991) 171–175, [https://doi.org/10.1016/0040-6090\(91\)90299-D](https://doi.org/10.1016/0040-6090(91)90299-D).
- [72] P.H. Mayrhofer, H. Willmann, C. Mitterer, Recrystallization and grain growth of nanocomposite Ti-B-N coatings, *Thin Solid Films* 440 (2003) 174–179, [https://doi.org/10.1016/S0040-6090\(03\)00858-7](https://doi.org/10.1016/S0040-6090(03)00858-7).
- [73] R. Daniel, D. Holec, M. Bartosik, J. Keckes, C. Mitterer, Size effect of thermal expansion and thermal/intrinsic stresses in nanostructured thin films: experiment and model, *Acta Mater.* 59 (2011) 6631–6645, <https://doi.org/10.1016/j.actamat.2011.07.018>.
- [74] J. Almer, M. Odén, L. Hultman, G. Håkansson, Microstructural evolution during tempering of arc-evaporated Cr-N coatings, *J. Vac. Sci. Technol. A Vacuum, Surfaces, Film.* 18 (2000) 121–130, <https://doi.org/10.1116/1.582128>.